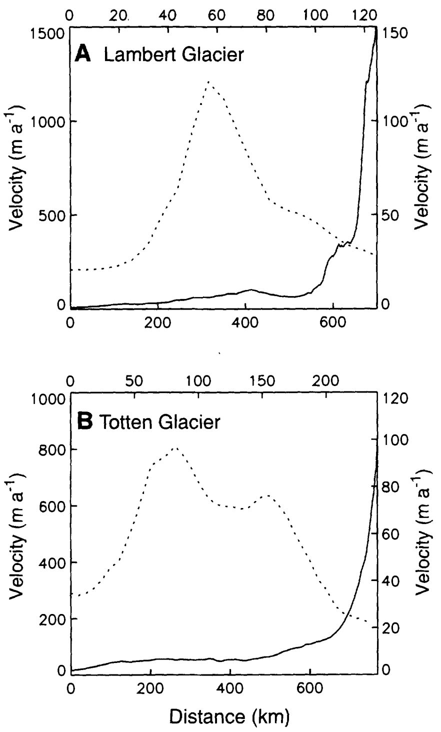

Fig. 4. Balance velocity profiles down two fast-flow features (**A** and **B**) in East Antarctica, the locations of which are shown by the white lines in Fig. 2, B and C. Transects running across each flow feature (dashed lines) are plotted with scales displayed on the right-hand ordinate and the upper abscissa. To avoid including floating ice, the profiles stop short of the estimated grounding line positions (*23*).

and inland flow represent, therefore, end members of a continuum of flow states within an ice sheet. This continuum of flow states is observed extensively in East and West Antarctica. It is also interesting to note that this type of behavior is not seen solely in Antarctica. A recently discovered ice stream in northeast Greenland (*21*) shows characteristics similar to those described above, and tributary-type flow is also present (*12*). It is likely, therefore, that former large ice masses, such as the Laurentide Ice Sheet, also possessed these flow characteristics.

This evidence challenges the view that the Antarctic plateau is a slow-moving and homogeneous region. Numerical models of the ice sheet have yet to reproduce the pattern and the complexity of flow shown in Fig. 2, therefore suggesting a limitation of their ability to simulate the present-day dynamics and future changes in the behavior of the largest ice mass on Earth.

References and Notes

1. C. R. Bentley, *J. Geophys. Res.* **92**, 8843 (1987).
2. R. Bindschadler, P. Vornberger, D. Blankenship, T. Scambos, R. Jacobel, *J. Glaciol.* **42**, 461 (1996).
3. T. J. Hughes, *Rev. Geophys. Space Phys.* **15**, 1 (1977).
4. S. J. Marshall and G. K. C. Clarke, *J. Geophys. Res.* **102**, 20615 (1997).
5. A. J. Payne, *Geophys. Res. Lett.* **25**, 3173 (1998).
6. ———, *Clim. Dyn.* **15**, 115 (1999).
7. N. F. McIntyre, *J. Glaciol.* **31**, 99 (1985).
8. I. Joughin *et al.*, *Science* **286**, 2833 (1999).
9. W. F. Budd and R. C. Warner, *Ann. Glaciol.* **23**, 21 (1996).
10. J. L. Bamber and R. A. Bindschadler, *Ann. Glaciol.* **25**, 439 (1997).
11. W. S. B. Paterson, *The Physics of Glaciers* (Pergamon, Oxford, ed. 3, 1994).
12. J. L. Bamber, R. J. Hardy, I. Joughin, *J. Glaciol.*, in press.
13. J. L. Bamber and P. Huybrechts, *Ann. Glaciol.* **23**, 364 (1996).
14. D. G. Vaughan, J. L. Bamber, M. Giovinetto, J. Russell, A. P. R. Cooper, *J. Clim.* **12**, 933 (1999).
15. D. J. Wingham, A. J. Ridout, R. Scharroo, R. J. Arthern, C. K. Shum, *Science* **282**, 456 (1998).
16. More information is available at the National Snow and Ice Data Center home page, www-nsidc.colorado.edu/NSIDC/.
17. M. Stenoien, thesis, University of Wisconsin–Madison (1998).
18. M. Jonas and D. G. Vaughan, *ERS-1 SAR Mosaic of Filchner-Ronee-Schelfeis*, Proceedings of the 11th International Workshop of the Filchner-Ronne Ice Shelf Programme, University of Stockholm, Sweden, 13 to 14 June 1996 (Alfred Wegener Institute, Bremerhaven, Germany, 1996).
19. J. F. Nye, *Geophys. J. R. Astron. Soc.* **7**, 431 (1963).
20. P. Huybrechts and J. Wolde, *J. Clim* **12**, 2169 (1999).
21. M. Fahnestock, R. Bindschadler, R. Kwok, K. Jezek, *Science* **262**, 1530 (1993).
22. D. J. Drewry, Ed., *Antarctica: Glaciological and Geophysical Folio* (Scott Polar Research Institute, Cambridge, 1983).
23. The assumptions about ice flow used to derive the balance velocities break down when the ice begins to float in the vicinity of the grounding line. Velocities close to the grounding line are, therefore, unreliable. Here, a simple test for whether the ice thickness was close to the value predicted by hydrostatic equilibrium was used to identify floating ice in Fig. 2.
24. We thank the European Space Agency for provision of the data used to produce the DEM and J. Dowdeswell for useful discussions on the text.

7 September 1999; accepted 21 December 1999

Density of Phonon States in Iron at High Pressure

R. Lübbers,[1] H. F. Grünsteudel,[2] A. I. Chumakov,[2] G. Wortmann[1]*

The lattice dynamics of the hexagonal close-packed (hcp) phase of iron was studied with nuclear inelastic absorption of synchrotron radiation at pressures from 20 to 42 gigapascals. A variety of thermodynamic parameters were derived from the measured density of phonon states for hcp iron, such as Debye temperatures, Grüneisen parameter, mean sound velocities, and the lattice contribution to entropy and specific heat. The results are of geophysical interest, because hcp iron is considered to be a major component of Earth's inner core.

The inner core of Earth is composed almost entirely of Fe or Fe-rich alloys. This geophysical aspect is one of the many motivations to study the phase diagram of Fe with its various isomorphs in a wide pressure and temperature range (*1*). The hcp high-pressure phase of Fe (ε-Fe) is considered the most relevant phase for the inner core (*2*). At ambient pressure and temperature, Fe is magnetic and crystallizes in the body-centered cubic (bcc) structure (α-Fe). The phase transformation of α-Fe to nonmagnetic ε-Fe at around 13 gigapascals (13 GPa) occurs over a broad pressure range depending on the sample environment (*3*). Although a considerable amount of crystallographic data on the pressure and temperature phase diagram of Fe is available (*1*), there is less experimental information available on the lattice dynamics of ε-Fe. The sound velocities in the ε-phase at high pressure and temperature are of particular interest, because seismic wave experiments indicate that the sound velocities in Earth's inner core are anisotropic (*4*).

The lattice dynamics of solids is described by phonons, which are characterized by their dispersion relations and by their density of states (DOS). Dispersion relations are conventionally measured with single-crystal samples using coherent inelastic neutron scattering (*5*). The phonon DOS can be obtained after adjusting the dispersion curves with a Born–von Kármán model (*6*). In special cases, incoherent neutron scattering can be used to determine the phonon DOS of polycrystalline samples (*5*). Alternatively, the density of phonon states of polycrystalline samples can be determined with the recently established technique of resonant nuclear inelastic absorption of synchrotron radiation (SR) (*7, 8*), which employed the 14.413-keV resonance of ^{57}Fe. Measurements of the phonon DOS in α-Fe (*9, 10*), Fe clusters (*11*), thin Fe layers (*12*), and Fe-containing quasicrystals (*13*) demonstrated the high sensitivity of this method. We used nuclear inelastic absorption to study a tiny (0.5 μg) Fe sample pressurized in a diamond anvil cell (DAC) and to measure the phonon DOS of ε-Fe.

The experiments were performed at the nuclear resonance station ID22N at the European Synchrotron Radiation Facility (ESRF),

[1]Fachbereich Physik, University of Paderborn, D-33095 Paderborn, Germany. [2]European Synchrotron Radiation Facility, Boite Postal 220, F-38043 Grenoble, France.

*To whom correspondence should be addressed. E-mail: wo_gw@physik.uni-paderborn.de

in Grenoble, France. The storage ring was operated in the 16-bunch mode, yielding a time window of 176 ns between the SR pulses. The experimental setup (Fig. 1) allows two types of nuclear resonance experiments distinguished by their coherent or incoherent character, with the latter arising from the transfer of energy to or from the lattice.

In the first type of experiments, named nuclear forward scattering (NFS), resonantly absorbed 14.413-keV gamma rays are scattered by the sample strictly in the forward direction and are detected by the first avalanche photodiode (APD1). For this purpose, the high-resolution monochromator is tuned to the nuclear resonance energy of ^{57}Fe, and the coherently forward scattered intensity is registered as a function of time with respect to the exciting SR pulses (*14*). This time analog to the classical Mössbauer effect allows the measurement of hyperfine interactions, used here to monitor the magnetic (α-Fe) or nonmagnetic (ε-Fe) state of the sample (*15*).

In the second experiment type, nuclear inelastic absorption spectra are measured by tuning the high-resolution monochromator in a range of about ± 100 meV around the nuclear resonance energy and monitoring the yield of a secondary radiation, here the Fe K_α (6.4 keV) and K_β (7.1 keV) x-ray fluorescence, in the time window between the SR pulses. The Fe x-rays are produced by the internal conversion process, which is the dominant deexcitation channel in the decay of the 14.413-keV level (*16*). For a given energy transfer, determined by the difference in energy of the incident radiation and the nuclear resonance, phonon states with any momentum allowed by the dispersion relations contribute equally to the absorption probability (*8, 10*). Thus, nuclear inelastic absorption provides momentum-averaged information on the density of the phonon states. Because of the incoherent nature of the absorption process, the Fe x-rays are emitted in arbitrary directions and are monitored by the two other detectors (APD2 and APD3), placed perpendicular to the beam and near to the pressurized sample by using a specially designed high-pressure cell with large openings for the APD detectors. In these measurements, the first detector (APD1) provides, by the forward-scattered 14.413-keV quanta, the spectrometer function. Further details may be found in (*10*).

The sample, an Fe foil (*17*) 90 μm in diameter and 10 μm thick, was placed between two diamonds, together with ruby chips (for pressure calibration with an accuracy of 5%), inside the hole of a gasket, with a mixture of methanol, ethanol, and water as a pressure-transmitting medium (*18*). Important factors for this high-pressure study were (i) the large cross-section of nuclear resonant absorption, which for the case of ^{57}Fe is several orders-of-magnitude larger than corresponding neutron or x-ray cross sections, (ii) the use of focusing optics (Fig. 1) that concentrated the monochromatized SR beam with a bandwidth of about 6 meV and a flux of 3×10^9 photons/s onto an area 100 μm by 100 μm, (iii) the complete suppression of any electronically (nonresonant) scattered background from the high-pressure environment by monitoring only delayed radiation from the nuclear decay, and (iv) the use of beryllium as the gasket material to allow sufficient transmission of the $K_{\alpha,\beta}$ x-rays.

The measurements were performed at room temperature (294 K) and at ambient pressure for α-Fe and 20, 32, and 42 GPa for ε-Fe. At 20 GPa and higher, the NFS spectra revealed the nonmagnetic phase of Fe (*15*), confirming a complete structural transition to ε-Fe. The normalized energy spectra of nuclear absorption (Fig. 2) consist of a central peak originating from elastic absorption and sidebands resulting from inelastic absorption with concomitant annihilation (left side) or creation (right side) of phonons. The spectrum of α-Fe is shown with the corresponding spectrum calculated with the phonon DOS from neutron scattering (*19*) and convoluted with the present spectrometer function (solid line in Fig. 2). The two data sets are compared in absolute scale without any adjustable parameter, demonstrating agreement between the two methods.

The procedure to extract the phonon DOS from the measured energy spectra of inelastic nuclear absorption was introduced by Sturhahn *et al.* (*8*). The multiphonon contributions and the central elastic peak were subtracted from the measured spectrum. The remaining spectrum represents the single phonon contribution, from which the density of phonon states $g(E)$ was extracted (*8, 20*). The resulting phonon DOS of α-Fe at ambient pressure and of ε-Fe at 42 GPa are shown in Fig. 3. The DOS of α-Fe is again well described by the solid line representing the DOS derived from neutron scattering (*19*). All spectral features of the DOS of ε-Fe are shifted to higher energies with respect to α-Fe. The resolved high-energy maximum of the DOS, originating mainly from longitudinal acoustic (α-Fe) and longitudinal acoustic and optical (ε-Fe) phonon branches, is shifted from 35 meV in α-Fe at ambient pressure to 51 meV in ε-Fe at 42 GPa.

The observed changes in the phonon spectra reflect primarily the reduced volume of the unit cell; modifications resulting from the structural transition are small for mono-atomic lattices (*21*) and are not resolvable with the present energy resolution, which is, however, sufficient to derive a set of thermodynamic parameters from the integral properties of the phonon DOS. The Lamb-Mössbauer factor f_{LM}, describing the elastic (recoil-free) fraction of the nuclear absorption, was calculated from the DOS according to (*9, 10, 20*). The results are given in Table 1, together with the

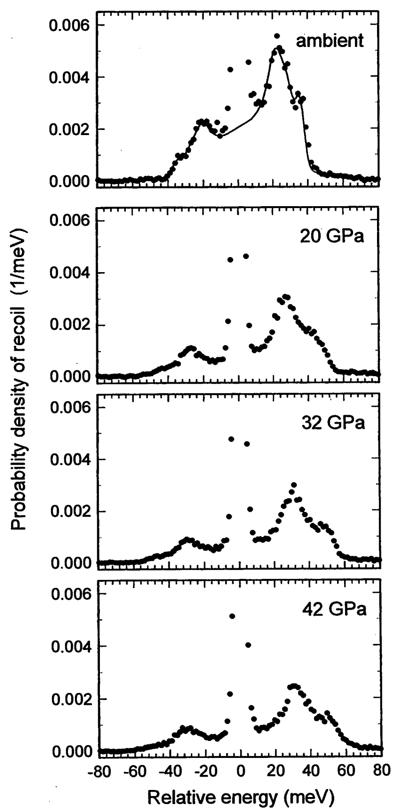

Fig. 2. Energy dependence of nuclear inelastic absorption of SR in Fe at different pressures. The spectra are normalized according to the procedure in (*8*). The intensity of the inelastic sidebands is proportional to $(1 - f_{LM})$; it decreases with increasing pressure by about 50%, reflecting the change in the recoil-free fraction, f_{LM}, from 0.80 to 0.90 (Table 1). The solid line shown in the uppermost spectrum is calculated from neutron data of α-Fe (*19*), convoluted with the spectrometer function.

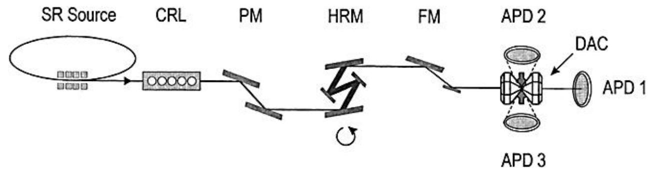

Fig. 1. Experimental setup. SR source: storage ring with two undulators tuned to 14.413 keV; CRL: focusing compound refractive lens (*33*); PM: high-heat load Si(1,1,1) double-crystal premonochromator with 3-eV bandwidth; HRM: nested high-resolution monochromator composed of two channel-cut Si(4,2,2) and Si(12,2,2) crystals with ~6-meV bandpass; FM: horizontally focusing Si(1,1,1) crystal pair (*34*); DAC: diamond anvil cell with beryllium gasket; APD1, APD2, APD3: avalanche photodiode detectors to monitor nuclear forward scattering and nuclear inelastic absorption.

Table 1. Thermodynamic parameters of Fe (*17*) derived from the densities of phonon states (see text), where at. stands for atom. For comparison, the corresponding parameters derived from neutron data (*19*) are given in the first line. V/V_0: relative volume obtained from compressibility data of ε-Fe (*25*) with V_0 = 7.093 cm³/mol. The uncertainties given in parentheses correspond to the statistical accuracy of the data on the last digit.

Pressure (GPa)	V/V_0	f_{LM}	$\langle \Delta x^2 \rangle$ 10^{-3} Å^2	E_{av} (meV)	$\theta_D(E_{av})$ (K)	c_V (k_B/at.)	U_{vibr} (meV/at.)	S_{vibr} (k_B/at.)	D_{av} (N/m)	v_{av} (km/s)
0, neutron	1	0.801	4.15	27.2	421	2.71	83.6	3.07	173	3.54
0, present	1	0.802(3)	4.13(7)	28.0(5)	433(8)	2.70(4)	83.4(20)	3.00(5)	185(12)	3.57(10)
20	0.862	0.882(3)	2.35(7)	36.5(8)	565(12)	2.51(4)	90.0(20)	2.31(5)	320(15)	4.82(15)
32	0.828	0.893(3)	2.12(7)	38.7(8)	599(12)	2.44(4)	91.8(20)	2.12(5)	365(15)	5.00(15)
42	0.805	0.897(3)	2.03(7)	40.7(8)	630(12)	2.42(4)	93.0(20)	2.06(5)	388(15)	5.14(15)

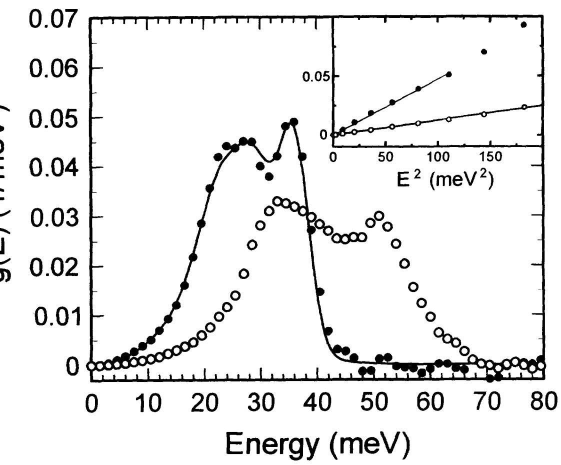

Fig. 3. Density of phonon states *g(E)* of α-Fe at ambient pressure (solid circles) and of ε-Fe at 42 GPa (open circles) obtained from the corresponding energy spectra in Fig. 2. The solid line represents the DOS from neutron scattering (*19*), convoluted with the spectrometer function. The inset shows a plot of the low-energy part of *g(E)* versus E^2 up to 15 meV in order to derive the sound velocity. Here, the solid lines represent a linear fit of the experimental data.

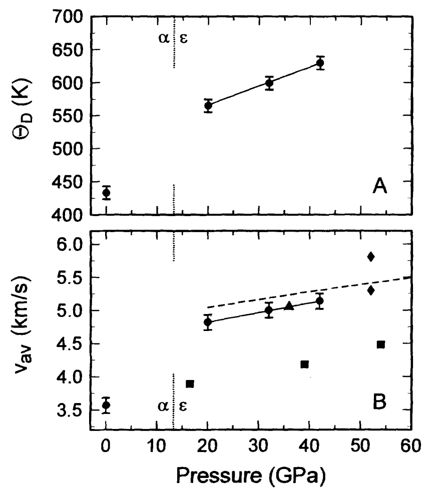

Fig. 4. Derived values of α-Fe and ε-Fe at room temperature (circles): (**A**) Debye temperature $\Theta_D(E_{av})$, (**B**) mean sound velocity v_{av}. Other experimental data in (B) are given by diamonds (*30*) and squares (*31*); theoretical calculations are indicated by a dashed line (*28, 31*) and a triangle (*29*). Solid lines are guides to the eye. The vertical dotted line indicates the center of the transformation of α-Fe to ε-Fe.

mean-squared thermal displacement $\langle \Delta x^2 \rangle$, determined by $f_{LM} = \exp(-k^2 \cdot \langle \Delta x^2 \rangle)$ with $k = 7.31 Å^{-1}$ as the wave vector of the 14.413 keV quanta. From the first moment of the DOS, we obtained a mean phonon energy E_{av} and, according to the Debye approximation, a corresponding Debye temperature $\Theta_D(E_{av}) = 4/3\ E_{av}/k_B$, where k_B stands for Boltzmann's constant (*22*).

By integration of the phonon DOS with various energy weights (*23*), we derived further thermodynamic properties such as the lattice contribution to the specific heat at constant volume c_V, the internal energy U_{vibr}, and the entropy S_{vibr}, as well as the mean force constant D_{av} (Table 1). Finally, from the low-energy part of the DOS up to 10 (α-Fe) and 15 meV (ε-Fe), where one can assume a linear relation between the phonon frequency ω(k) and the lattice k-vector (*19*), we derived the average velocity of sound v_{av} (Fig. 3) according to the relation (*24*): $g(E) = \alpha E^2$, where $\alpha = V/2\pi^2\hbar^3 v_{av}^3$. Here, V stands for the volume per Fe atom and $\hbar$ for Planck's constant. In order to examine the reliability of all the derived parameters, we compared them with those from neutron data of α-Fe at ambient pressure (Table 1).

We now discuss the volume dependencies of the Debye temperature and the average velocity of sound shown in Fig. 4. The Debye temperature of Fe increases by almost 50% in the studied pressure range. The volume dependence of $\Theta_D(E_{av})$ is described by the Grüneisen parameter, defined as $\gamma = -d\ln\Theta_D/d\ln V$. With the present $\Theta_D(E_{av})$ data and the corresponding volumes (*25*), we derived γ(ε-Fe) = 1.5 ± 0.2. This value represents an average for the investigated pressure range (20 to 42 GPa) and is slightly lower than the measured value for α-Fe at ambient conditions γ(α-Fe) = 1.66 (*26*).

The value of the sound velocity in our α-Fe sample, v_{av} = 3.57 ± 0.10 km/s, is consistent with v_{av} = 3.54 km/s, derived in the same way using the phonon DOS from neutron data (*19*). In addition, the average sound velocity v_{av} can be compared with results derived, in the Debye approximation, from the longitudinal and transverse sound velocities v_p and v_s: $3(v_{av})^{-3} = (v_p)^{-3} + 2(v_s)^{-3}$. From tabulated values of v_p and v_s for Fe at ambient conditions (*27*), we obtained a mean value of v_{av} = 3.58 ± 0.03 km/s. Our experimental values of v_{av} in the ε-phase agree with theoretical calculations (*28, 29*) and an elasticity study (*30*), whereas data derived by recent ultrasound and elasticity studies (*31*) deviate by about 20% (Fig. 4B).

Finally, our data (for example c_V, U_{vibr}, and S_{vibr}) provide, in contrast to other (e.g., calorimetric) measurements, pure vibrational parts of the thermodynamic properties. They are free of the possible electronic or magnetic contributions from the 3*d* band electrons and are therefore useful for testing theoretical calculations of thermodynamic parameters responsible for the equation-of-state (*29*) or the melting temperature of Fe (*32*).

References and Notes

1. O. Anderson, *Science* **278**, 821 (1997), and references therein.
2. C. S. Yoo, J. Akella, A. J. Campbell, H. K. Mao, R. J. Hemley, *Science* **270**, 1473 (1995).
3. N. von Bargen and R. Boehler, *High Pressure Res.* **6**, 113 (1990).
4. K. C. Creager, *Nature* **356**, 309 (1992); *Science* **278**, 1284 (1997).
5. G. L. Squires, *Introduction to the Theory of Thermal Neutron Scattering* (Cambridge Univ. Press, Cambridge, 1978).
6. G. Gilat and L. J. Raubenheimer, *Phys. Rev.* **144**, 390 (1966).
7. M. Seto, Y. Yoda, S. Kikuta, X. W. Zhang, M. Ando, *Phys. Rev. Lett.* **74**, 3828 (1995).
8. W. Sturhahn *et al.*, *Phys. Rev. Lett.* **74**, 3832 (1995).
9. A. I. Chumakov, R. Rüffer, A. Q. R. Baron, H. Grünsteudel, H. F. Grünsteudel, *Phys. Rev. B* **54**, R9596 (1996).
10. A. I. Chumakov and R. Rüffer, *Hyperfine Interactions* **113**, 59 (1998).
11. B. Fultz, C. C. Ahn, E. E. Alp, W. Sturhahn, T. S. Toellner, *Phys. Rev. Lett.* **79**, 937 (1997).
12. R. Röhlsberger *et al.*, *Physica B* **263-264**, 581 (1999).
13. R. A. Brand, G. Coddens, A. I. Chumakov, Y. Calvayrac, *Phys. Rev. B* **59**, R14145 (1999).
14. J. B. Hastings, D. P. Siddons, U. v. Bürck, R. Hollatz, U. Bergmann, *Phys. Rev. Lett.* **66**, 770 (1991).
15. H. F. Grünsteudel *et al.*, *Aust. J. Phys.* **51**, 453 (1998).
16. By the internal conversion process, an electron from the K shell is emitted instead of the γ quantum; for ^{57}Fe, this process is more probable by a factor of 8.25 than

the γ-ray emission. The $K_{\alpha,\beta}$ x-rays originate from the subsequent filling of the holes in the K shell.
17. The Fe foil had a purity of 99.95% and was enriched to 95% in the ^{57}Fe isotope. Because the atomic mass of the probe atom is 57u and that of the lattice atoms is close to 57u (where u is the atomic mass unit), all results exhibit a systematic deviation from natural Fe (55.86u) in the range of 1 to 2%. This deviation is smaller than the present experimental uncertainty, however it should be considered in all studies with ^{57}Fe.
18. A. Jayaraman, *Rev. Mod. Phys.* **55**, 65 (1983).
19. V. J. Minkiewicz, G. Shirane, R. Nathans, *Phys. Rev.* **162**, 528 (1967). The DOS is tabulated by H. R. Schober and P. H. Dederichs, in *Landolt-Börnstein*, K.-H. Hellwege and J. L. Olsen, Eds. (Springer-Verlag, Berlin, 1981), vol. III/13a, pp. 53–56.
20. K. S. Singwi and A. Sjölander, *Phys. Rev.* **120**, 1093 (1960).
21. J. D. Althoff, P. B. Allen, R. M. Wentzcovitch, J. A. Moriarty, *Phys. Rev. B* **48**, 13253 (1993).
22. Debye temperatures can be calculated alternatively from the Lamb-Mössbauer factor, the low-temperature specific heat, or the low-energy part of the phonon DOS, thus providing slightly different data sets reflecting mainly deviations of the lattice dynamics from a perfect Debye-like behavior.
23. W. Jones and N. H. Marsh, *Theoretical Solid State Physics* (Dover, New York, 1985), vol. 1, p. 237.
24. V. G. Kohn, A. I. Chumakov, R. Rüffer, *Phys. Rev. B* **58**, 8437 (1998).
25. H. K. Mao, Y. Wu, L. C. Chen, J. F. Chu, A. P. Jephcoat, *J. Geophys. Res.* **95**, 21737 (1990).
26. J. Ramakrishnan, R. Boehler, G. H. Higgins, G. C. Kennedy, *J. Geophys. Res.* **83**, 3535 (1978).
27. G. Simmons and H. Wang, *Single Crystal Elastic Constants and Calculated Aggregate Properties* (MIT Press, Cambridge, MA, 1971). The described procedure of calculating v_p and v_s from elastic constants was used also for results from (*29, 30*).
28. L. Stixrude and R. E. Cohen, *Science* **267**, 1972 (1995); see also (*31*).
29. P. Söderlind, J. A. Moriarty, J. M. Wills, *Phys. Rev. B* **53**, 14063 (1996).
30. A. Singh, H.-K. Mao, J. Shu, R. J. Hemley, *Phys. Rev. Lett.* **80**, 2157 (1998).
31. H.-K. Mao *et al.*, *Nature* **396**, 741 (1998); *Nature* **399**, 280 (1999).
32. D. Alfè, M. J. Gillan, G. D. Price, *Nature* **401**, 462 (1999).
33. A. Snigirev *et al.*, *Nature* **384**, 49 (1996).
34. A. K. Freund *et al.*, *Proc. SPIE* **3448**, 1 (1998).
35. We thank the Microfluorescence group (ID22) and the Nuclear Resonance group (ID18) of the ESRF for preparation of nuclear resonance station ID22N and for their help during the experiment, A. Snigirev and A. K. Freund for their expert help with the focusing elements, and K. Rupprecht and H. Giefers for their assistance with the measurements. We acknowledge useful discussions with W. B. Holzapfel, R. Rüffer, G. Shen, and W. Sturhahn. Supported by the Bundesministerium für Bildung, Wissenschaft, Forschung und Technologie (project 05 SK8PPA).

11 November 1999; accepted 29 December 1999

Inhibition of Experimental Liver Cirrhosis in Mice by Telomerase Gene Delivery

Karl Lenhard Rudolph,[1] Sandy Chang,[1,2] Melissa Millard,[1] Nicole Schreiber-Agus,[3] Ronald A. DePinho[1]*

Accelerated telomere loss has been proposed to be a factor leading to end-stage organ failure in chronic diseases of high cellular turnover such as liver cirrhosis. To test this hypothesis directly, telomerase-deficient mice, null for the essential telomerase RNA (mTR) gene, were subjected to genetic, surgical, and chemical ablation of the liver. Telomere dysfunction was associated with defects in liver regeneration and accelerated the development of liver cirrhosis in response to chronic liver injury. Adenoviral delivery of mTR into the livers of $mTR^{-/-}$ mice with short dysfunctional telomeres restored telomerase activity and telomere function, alleviated cirrhotic pathology, and improved liver function. These studies indicate that telomere dysfunction contributes to chronic diseases of continual cellular loss-replacement and encourage the evaluation of "telomerase therapy" for such diseases.

Cirrhosis of the liver is the seventh leading cause of death by disease, affecting several hundred million people worldwide (*1*). In this chronic disease, a diverse array of hepatotoxins, ranging from chronic viral hepatitis to alcohol, promotes continual hepatocyte destruction that, in turn, stimulates abnormal patterns of hepatocyte regeneration and fibrous scarring over many years (*2*). The resulting distortion of the liver architecture compromises hepatocyte function, causing systemic life-threatening complications. Left unchecked, this pathological process culminates in fatal end-stage liver failure, marked by extensive fibrotic replacement and cessation of hepatocyte proliferation (*2, 3*).

Liver cirrhosis is characterized by the conversion of hepatic stellate cells into activated, myofibroblast like cells (*2*). It has been postulated that hepatocyte destruction itself serves as an activation signal for this conversion, possibly by the release of insulin-like growth factor or lipid peroxides from apoptotic cells (*2*). Therefore, factors that govern the survival of hepatocytes could potentially influence stellate cell activation and fibrogenesis.

The second key aspect of terminal liver failure, hepatocyte proliferative arrest, has been linked to several etiologic factors including altered hepatocyte-matrix interactions (*2*), growth inhibition by abundant transforming growth factor–β1 (TGF-β1) (*4*), and/or critical telomere shortening. The telomere hypothesis is a particularly appealing one, because sustained hepatocyte turnover accelerates the pace of telomere attrition in the human cirrhotic liver (*5*), thereby presumably activating senescence or crisis checkpoints. The importance of telomere maintenance in long-term cellular and organ homeostasis has been experimentally verified in cultured human cells and in telomerase-deficient mice (*6, 7*). These mice lack the telomerase RNA (mTR) gene and show progressive telomere shortening from one generation to the next. In late-generation mice (e.g. generation 6), telomere dysfunction and genomic instability are associated with impaired proliferation and/or apoptosis in organ systems with high renewal requirements, such as the bone marrow and the gut (*8*). In contrast, the liver is unperturbed and appears to function and develop normally even in late-generation $mTR^{-/-}$ mice (*9*). Here we use the $mTR^{-/-}$ mice to evaluate the role of telomere shortening in chronic liver disease. Liver injury was induced in these animals by three experimental procedures to gauge how telomere shortening influences hepatocyte proliferation, survival, and ultimately predisposition to cirrhosis.

The first system, the albumin-directed urokinase plasminogen activator (Alb-uPA) transgenic mouse, allows investigation of the factors governing hepatocyte regenerative capacity. Alb-uPA expression has been shown to cause widespread hepatocyte death and liver failure in newborn mice (*10*). However, 60% of hemizygous transgenic mice survive as a result of spontaneous transgene deletion in rare hepatocytes that then clonally expand to reconstitute the entire organ by 3 months of age (*11*). To assess the impact of loss of telomerase activity and telomere shortening on liver regeneration capacity, we monitored Alb-uPA transgene transmission as well as phenotypic differences in $mTR^{+/+}$ mice and successive generations of $mTR^{-/-}$ mice (*12*). Consistent with previous reports (*11*), we observed transmission rates of 31% for $mTR^{+/+}$ and 27% for second-generation (G2) $mTR^{-/-}$ mice (Fig. 1A). Because the

[1]Department of Adult Oncology, Medicine and Genetics, Dana-Farber Cancer Institute, 44 Binney Street (M413), and Harvard Medical School, Boston, MA 02115, USA. [2]Department of Pathology, Brigham and Women's Hospital and Harvard Medical School, Boston, MA 02115, USA. [3]Department of Molecular Genetics, Albert Einstein College of Medicine, Bronx, NY 10461, USA.

*To whom correspondence should be addressed. E-mail: ron_depinho@dfci.harvard.edu